Dual CP Polarization Diversity and Space Diversity Antennas Enabled by a Compact T-shaped Feed Structure

Junping Geng[1], Senior Member, IEEE, Richard W. Ziolkowski[2,3], Fellow, IEEE, Kun Wang[1], Han Zhou[1], Guanshen Chenhu[1], Xianling Liang[1], Senior Member, IEEE, Ronghong Jin[1], Fellow, IEEE

[1]Department of Electronics Engineering, Shanghai Jiao Tong University, Shanghai 200240, China
[2]The University of Technology Sydney, Global Big Data Technologies Centre, Ultimo NSW 2007, Australia
[3] The University of Arizona, Department of Electrical and Computer Engineering, Tucson, AZ 85721 USA

Corresponding author: Junping Geng, (e-mail: gengjunp@sjtu.edu.cn).

ABSTRACT A compact T-shaped feed structure (TFS) is reported that enables the realization of two types of diversity antennas: a polarization diversity antenna (PDA) and a spatial diversity antenna (SDA). Both systems have a high potential for mobile wireless communication applications. The TFS includes four ports and two independent coaxial channels with effective isolation between them all. The PDA is a dual CP omnidirectional antenna. Its optimized prototype achieves measured impedance bandwidths of 16.4% and 15.28% in its LHCP and RHCP states, respectively, and realized gains in both between 4.8 to 6.46 dBic. The inner thin coaxial cable (ITCC) of the TFS directly drives its LHCP subsystem, facilitating its improved omnidirectional performance. This ITCC is also used to directly feed the SDA's low-profile directional planar equiangular spiral antenna and its side port drives its omnidirectional RHCP antenna. Good hemispherical coverage is realized with a measured common impedance bandwidth larger than 14.35% with more than 40 dB isolation between its two ports. The corresponding measured realized gain of the SDA is between 4 and 7.8 dBic. The measured results for both optimized prototypes confirm their simulated performance characteristics.

INDEX TERMS Dual CP omnidirectional antenna (DCPOA), internal thin coaxial cable (ITCC), omnidirectional CP slot array antenna (OCPSA), polarization diversity antenna (PDA), spatial diversity antenna (SDA), T-shaped feed structure (TFS).

I. INTRODUCTION

With the rapid development of mobile wireless communication systems, such as wireless ad hoc networks, there has been strong interest in polarization diversity (PDA) and spatial diversity (SDA) antennas. Polarization diversity is a good method to overcome channel fading in complex wireless environments. Independent signals can be transferred in different polarization states in the same space channel. This raises the channel efficiency and increases the wireless communication capacity [1]-[3]. Moreover, spatial (e.g., pattern) diversity facilitates more flexible space coverage. It supports more signal channels that can be combined to realize high quality communications and provides more flexibility in different scenarios. Circular polarization (CP) characteristics are very important for the realization of these polarization and pattern diversity properties. Different beams work in different directions for wider coverage, and suppress the interference between different ports and modes.

These PDA and SDA antennas are of particular interest for mobile terminals that not only communicate with neighbouring nodes, but also connect to satellite or unmanned aerial vehicles (UAVs) [4], [5]. These antennas usually have two orthogonal ports or a single port with switches. Hemispherical coverage, high gain and large angle CP beams are necessary features for these moving platforms, e.g., a vehicle communicating in an ad hoc wireless network [4]-[6]. Considerable research on antenna diversity has led to increasing the channel capacity and overcoming multipath fading [7]-[9].

An omnidirectional RHCP antenna that combined monopole and loop radiators was designed in [10]. The 3-dB axial-ratio (AR) bandwidth was 17.5%, ranging from 1.46 to 1.74 GHz, in the azimuthal plane. Its gain was 0.86

dBic. A broadband omnidirectional antenna with dual CP performance was achieved by adopting right-hand (RHCP) and left-hand (LHCP) CP elements on the upper and lower parts of a cylinder [11]. In [12], a compact-size low-profile wideband patch antenna was reported that achieved a polarization reconfigurable property with PIN diodes across a slot. As a consequence, it had increased insertion loss and required additional complex biasing circuits.

To achieve omnidirectional CP radiation with higher gain in the horizontal plane, a series of coaxial slot array antennas were reported in [13]-[18]. Omnidirectional CP antennas based on a coaxial cylinder waveguide with slot arrays positioned around its conducting shell were first proposed [13]. Four orthogonal slots pairs separated by a half wavelength interval were arranged to radiate an omnidirectional CP field. The antenna had a -10-dB impedance bandwidth, axial ratio (AR) values < 3 dB, and 6.5 dBic peak gain from 5.1 to 5.9 GHz. It was further demonstrated that larger gain could be achieved with more slots [14]. Nevertheless, the omnidirectional CP antenna in [13], [14] only had a single feeding port and, hence, only radiated RHCP fields.

A dual-CP omnidirectional antenna was developed in [15] that had one port at each end of the coax structure to realize the dual CP property. These two ports excited omnidirectional LHCP and RHCP waves, respectively. However, it was found that connecting the feed wire to the LHCP port from the outside negatively affects the radiation pattern when the antenna is mounted vertically on the roof of a metallic vehicle. As a result, it does not achieve omnidirectional radiation and its CP characteristics are lost in some azimuth directions.

A related truncated circular cone, slot array antenna was developed in [17]. It was fed from a bottom port and the resulting guided wave excited its throat ring, which then radiated a conical CP beam. The direction of the conical beam depended on the vertex angle of the outer conductor and the proper arrangement of the positions of its two slot arrays. A T-shaped feed structure was proposed in [18] to feed a multi-port antenna system. It exhibited high isolation between its two channels and a notable small insertion loss in its transmission channel.

A coaxial T-shaped feed structure (TFS) with 4 ports is developed in this paper. It facilitates a radiating system that combines an omnidirectional CP slot array antenna (OCPSA) with polarization and spatial diversity antennas. The TFS is a greatly improved version of the design in [18]. It is compact and realizes two independent, effectively isolated channels. It is combined with an omnidirectional CP slot array antenna (OCPSA) to realize an improved dual CP omnidirectional antenna (DCPOA). This PDA is fed from only two ports of the TFS and radiates both LHCP and RHCP fields. The improved DCPOA is very useful since it achieves omnidirectional CP diversity when it is vertically mounted on the top of a vehicle. The TFS is also used to realize a wideband spatial diversity antenna (SDA). An internal thin coaxial cable (ITCC) embedded in the center

of the structure replaces the inner metal wire of the OCPSA employed in [13]-[16]. One channel of the TFS feeds its OCPSA; another channel is connected through the ITCC to a low profile directional antenna mounted on top of it. This arrangement realizes horizontal omnidirectional fields and fields radiated directionally upwards. Prototypes of both of the PDA and SDA were fabricated and measured. The simulated performance characteristics of both were confirmed.

II. T-shaped feed structure
The TFS was designed and simulated using the commercially available CST Microwave Studio simulation software. The time domain finite-integration (FIT) and finite difference time domain (FDTD) algorithms were used for the time domain simulations; the finite element (FEM) package was used for related frequency domain simulations [19], [20].

In comparison to other multiport networks, the reported feeding structure is compact and its two electromagnetic channels are completely isolated physically. It is used to feed the dual CP antenna or space diversity antenna from their down sides. This mitigates the negative effect of any feeding wire connected to the top port. Consequently, the PDA or SDA can be mounted very conveniently on the top of a car.

A. TFS geometry

The TFS is constructed with coaxial structures. It is shown in Fig. 1. Two physically separated channels are realized for the electromagnetic power flows. One channel is the internal thin coaxial cable (ITCC) with input at port 1 and output at port 3. It has a 50 Ω characteristic impedance. This arrangement is shown in Fig. 1(b). Port 1 is connected to a standard SMA adaptor connector. Port 3 is extended to the antenna. The other channel is from port 2 to port 4, as depicted in Fig. 1(c). It acts like a bent coaxial wire with a parallel coaxial short branch. The feed wire connected to port 2 is designed as a coaxial tapered wire with a stable characteristic impedance. A standard SMA connector is combined with port 2. A horn-shaped piece of coaxial wire is connected with port 4. Port 4 is then connected with the radiating portion of an orthogonal slot array. The equivalent circuit of the channel from port 2 to port 4 is shown in Fig. 1(d). When port 2 is excited, power flows to port 4. Its bottom end is shortened by a metal ring (indicated by the red piece shown in Figs. 1(a) and 1(b)). This ring reflects the input wave incident on it back to port 4. The length l_1 is arranged to ensure that the combined electromagnetic power has the same phase at port 4. It is clear that the vertical distance l_1 between port 1 and port 2 is essential to increase the transmission efficiency between port 2 and port 4, and to improve the energy distribution at port 4.

It is also clear that a high isolation between the two channels is obtained by their physical separation. Ports 1 and 2 are each connected directly to a standard SMA connector. The medium filling the TFS is Teflon with $\varepsilon_r = 2.1$.

B. TFS impedance transformation

The impedance of the feeding structure connected with port 4 is not stable without careful design. Because some of the
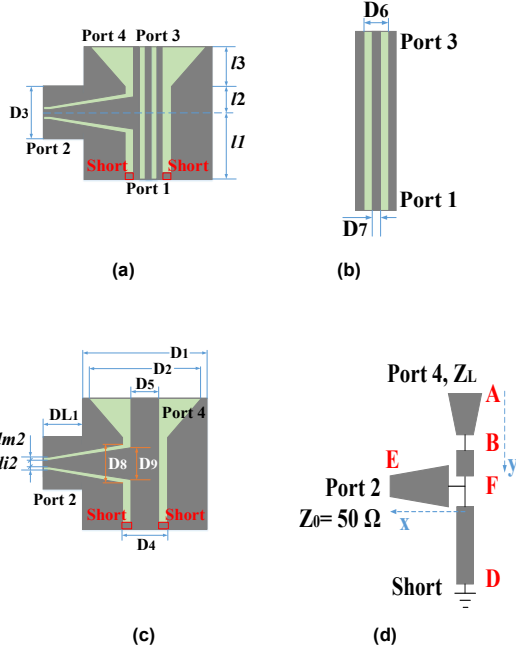

FIGURE 1. The T-shaped feed structure (TFS). (a) A cross-sectional view through a vertical cut. (b) Port 1 is connected directly to port 3 by a coaxial line. (c) The channel connects port 2 and port 4 with a bent coaxial cable and a shortened parallel horn-shaped coaxial branch. (d) Equivalent circuit of (c). The signal enters from port 2 and flows to port 4, when port 1 is shortened.

power input into port 2 will flow towards the ring, as well as to port 4, it is clear that the correct length of the shortened branch is essential to an effective functioning of the system. Moreover, the small sized coaxial waveguide is connected to the large radiation part of the OCPSA. Consequently, it must be configured properly to achieve good impedance matching.

Assume the load to port 4 is Z_L, as shown in Fig. 1(d). The characteristic impedance of the tapered coaxial cable of part AB is

$$Z_c(y) = \frac{60}{\sqrt{\varepsilon_r}} \ln \frac{2}{D_5} \left[\frac{D_2 - D_4}{2l_3}(l_3 - y) + D_4 \right] \tag{1}$$

Here, ε_r is the permittivity of Teflon, the medium filling the coaxial cable. The other size parameters are noted in Fig. 1. According to the impedance transformation associated with a tapered transmission line, the impedance at y+dy in part AB is

$$Z_{in}(y + dy) = Z_c(y) \frac{z_{in}(y) + jz_c(y)tan(\beta dy)}{z_c(y) + jz_{in}(y)tan(\beta dy)} \tag{2}$$

If $dy \to 0$, Eq. (2) can be simplified to be

$$Z_{in}(y + dy) \cong Z_{in}(y) + Z'_{in}(y)dy \tag{3}$$

From A to B, the impedance $Z_L = Z_{in}(y = 0)$ is transformed to be

$$Z_{in}(y = l_3) = Z_{in}(y = 0) + \int_0^{l_3} Z'_{in}(y)\,dy \tag{4}$$

For the uniform coaxial transmission line, part BF, the characteristic impedance is

$$Z_c(BF) = \frac{60}{\sqrt{\varepsilon_r}} \ln \frac{D_2}{D_5} \tag{5}$$

From B to F, the impedance $Z_{in}(y = l_3)$ is transformed to be

$$Z_{F1}(y = l_3 + l_2) = Z_c(BF)\frac{z_{in}(y=l_3) + jz_c(BF)tan(\beta l_2)}{z_c(BF) + jz_{in}(y=l_3)tan(\beta l_2)} \tag{6}$$

The uniform coaxial transmission line, part DF, is shorted at D. The characteristic impedance $Z_c(DF)$ is the same as $Z_c(BF)$. Consequently, the impedance is transformed by part DF to be Z_{F2} at position F.

$$Z_{F2} = jZ_c(DF)tan(\beta l_1) \tag{7}$$

where Z_{F1} and Z_{F2} are a parallel combination so that $Z_F = Z_{F2}//Z_{F1}$.

Part FE is also a tapered coaxial transmission line. Its characteristic impedance is

$$Z_c(x) = \frac{60}{\sqrt{\varepsilon_r}} \ln \frac{D_8 \cdot (D_1 - D_5 + 2DL_1)}{D_9 \cdot (D_1 - D_4 + 2DL_1)} = Z_{c0} \tag{8}$$

According to the impedance transformation of the tapered transmission line, the impedance at x+dx in part FE is

$$Z_{in}(x + dx) = Z_{c0} \frac{Z_{in}(x) + jZ_{c0}tan(\beta dx)}{Z_{c0} + jZ_{in}(x)tan(\beta dx)}$$
$$= Z_{in}(x) + Z'_{in}(x)dx \tag{9}$$

From point F to E, the Z_F is then transformed to be

$$Z_{in}\left(E, x = DL_1 + \frac{D_1}{2}\right) = Z_F + \int_0^{DL_1 + \frac{D_1}{2}} Z'_{in}(x)dx \tag{10}$$

Since it is connected to the 50 Ω SMA adaptor at port 2,

$$Z_{in}\left(E, x = DL_1 + \frac{D_1}{2}\right) = 50\ \Omega \tag{11}$$

If the load Z_L is known at port 4, we can then solve the above equations to determine the size parameters of the TFS. We assume $Z_L = 100\ \Omega$ at port 4 and then determine the initial parameter size of the TFS. An explicit model was constructed next in CST and was then optimized by simulation.

C. TFS performance

From the simulation results in Fig. 2, we find that the length l_1 affects the impedance matching across the entire operational band because it impacts the impedance transformation from the shorted end. It is found by optimization that $l_1 = 17$ mm. The simulated reflection coefficient at port 2, $|S_{22}| < -10$ dB, is from 2.31 to 8.95 GHz. Within the same band, the isolation coefficient $|S_{12}|$ between the two input ports is below -30 dB and $|S_{42}|$ is higher than -0.5 dB between 2.33 to 8.93 GHz.

The magnitude of $|S_{22}|$, will deteriorate if l_1 is 12 mm. Both $|S_{22}|$ and $|S_{42}|$ will deteriorate significantly if l_1 deviates from 17 mm. The length of the coaxial tapered line can also
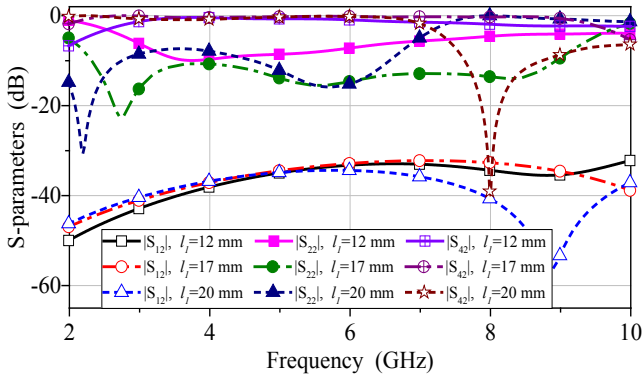

FIGURE 2. S parameters when *l*1 = 12, 17, and 20 mm.

affect the performance because it controls the phase difference between the waves guided in the two channels. If l_1 is changed from its optimized value, the impedance-match band of the TFS deviates from the original band and the operational bandwidth of the antenna system will become narrower.

III. TFS-fed improved dual CP omnidirectional antenna

Polarization diversity means the antenna can change its polarization if it is necessary. This feature can overcome de-polarization, improve the stability of the channel, and increase the capacity of the communications. It has been demonstrated that the OCPSA has dual-CP omnidirectional radiation performance when it is upright and fed from its top port or its bottom ports [15]. However, the feed cable to the top port was originally hung on the side of the antenna and, as a consequence, broke the omnidirectional pattern and deteriorated the CP performance in practice. Here, the TFS provides an improved feeding of the DCPOA.

A. The principle and structure of the improved DCPOA

The improved DCPOA mainly consists of two parts: a coaxial cylinder structure with slot arrays and the TFS. As discussed in [15], the right or left hand CP properties are obtained when the slots pairs are excited from different ports.

The improved DCPOA is fed by the TFS as illustrated in

Fig. 3. The TFS itself is the feed network shown in Fig. 3(a). Port 1 connects port 3 to feed the LHCP antenna; Port 2 connects port 4 to feed the RHCP antenna. As shown in Fig. 3(b), port 1 on the bottom excites the LHCP radiation, and port 2 on the side excites the RHCP wave. This configuration yields the improved performance only if the isolation between them is high enough. Furthermore, the ITCC replaces the core metal wire of the OCPSA in [13]. The inner core metal wire of the ITCC is connected to the top cap of the improved DCPOA as shown in Fig. 3(c).
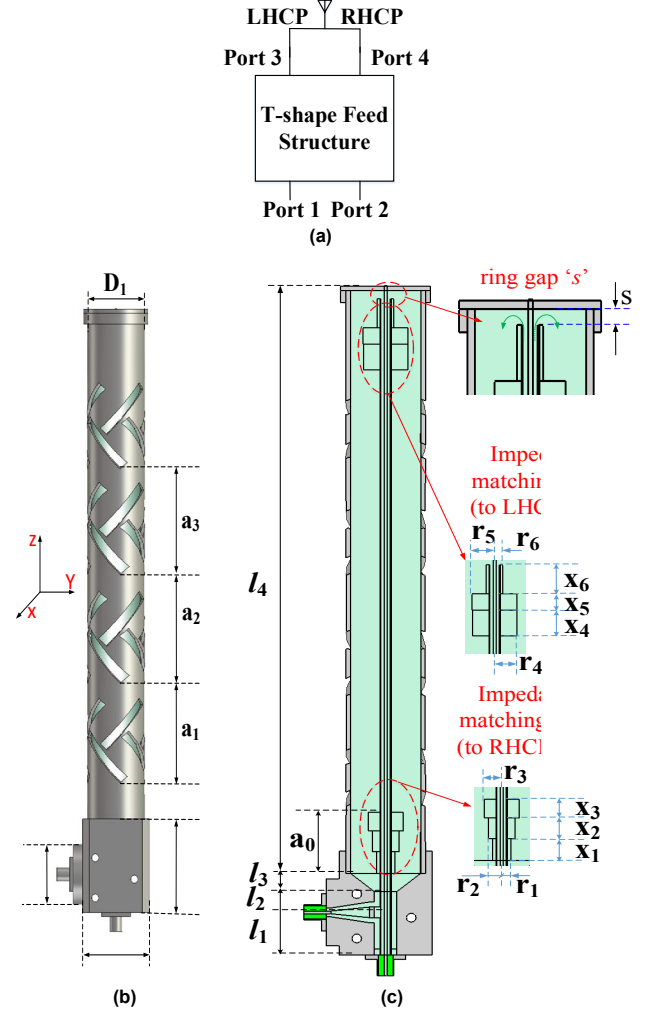

FIGURE 3. The T-shaped fed dual-CP slot arrays antenna. (a) Overview diagram. (b) 3D view. (c) Cross-sectional view through a vertical cut.

There is a small ring gap 's' between the top cap and the outer conductor of the ITCC as shown in Fig. 3(c).

Port 1 of the TFS directly feeds the ITCC in order that a TEM wave is transmitted along the ITCC to the top of the antenna, which then propagates out of the ring gap 's'. It also channels the fields downward between the ITCC and the outer conductor shell with its slot arrays. The LHCP wave is then radiated out into free space. The TEM wave being excited from port 2 propagates into the original

coaxial slot array antenna and transmits from the bottom to the top, radiating RHCP fields from it.

B. Performance of the improved DCPOA

The characteristic impedances of port 1 on the bottom and port 2 on the side are designed to be 50 Ω. Thus, SMA connectors can be attached to them directly. When port 1 (LHCP) is excited and port 2 (RHCP) is terminated with a 50 Ω load, the antenna generates the LHCP radiation. On the other hand, the RHCP field is radiated when port 2 is excited and port 1 is terminated with a 50 Ω load.

The ITCC runs through the entire antenna and serves as a channel for power to flow from its bottom to its top. The combination of the outer conductor of the ITCC and the outer shell of the antenna also serves as another coaxial cylinder that facilitates power propagating from the top of the antenna to its bottom. Details of the connection between the two coaxial structures can be seen in Fig. 3(c). The inner conductor of the ITCC is extended the distance $s =$ 2.9 mm to be connected to the top metal cap of the antenna. The consequence is the presence of a ring gap 's' between the outer conductor of the ITCC and the top metal cap.

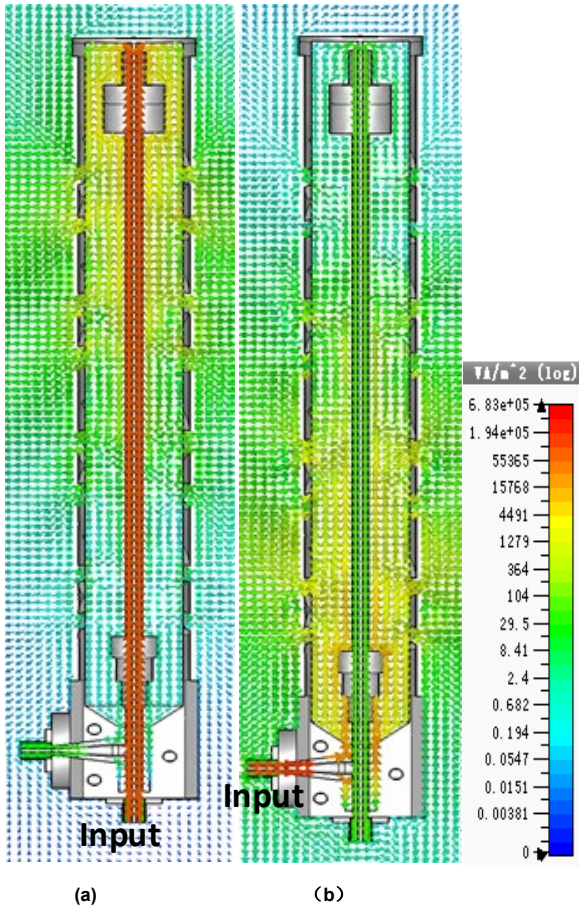Fig. 4(a) shows the power propagating through the ITCC

FIGURE 4. Power flow in the structure. (a) When fed from the LHCP port 1. (b) When fed from the RHCP port 2.

from its bottom to its top until it arrives at the metal cap.

This occurs when the LHCP port 1 is excited. This power then propagates out of the ring gap 's'- the throat of the channel - and enters into the outer coax cylinder structure and flows from the top to its bottom. The slot pairs are around this outer structure. Leaky waves are then radiated out from them. Only a very minor amount of this power is left in the channel; it propagates down to the RHCP port 2.

When the RHCP port 2 is excited, the power propagates through the outer coaxial cylinder from its bottom to its top. Leaky wave fields are then radiated from the slots pairs into free space. The power flow distribution is illustrated in Fig. 4(b). It shows that the three lower rings of the slot pairs radiate most of the energy, the last one radiating only a very minor amount of the power. This behavior also means that the last circle of slots makes only a minor contribution to the gain of the antenna. Moreover, it also means that the isolation between port 1 and port 2 is very high.

To further increase the radiation efficiency of the LHCP antenna, three metal rings as shown in Fig. 3(c) were inserted around the ITCC to match the impedance. This choice is similar to the one taken in [15]. These rings are close to the top cap and have the lengths x_4, x_5 and x_6, respectively, denoted from the first one to the top most ring. Those lengths were calculated and optimized with an equivalent circuit of the impedance of the LHCP antenna. Similar to the RHCP antenna, three additional metal rings were inserted around the ITCC, close to the TFS, to match the impedance of the RHCP antenna. Their lengths are x_1, x_2 and x_3, respectively, denoted from the bottom ring upwards.
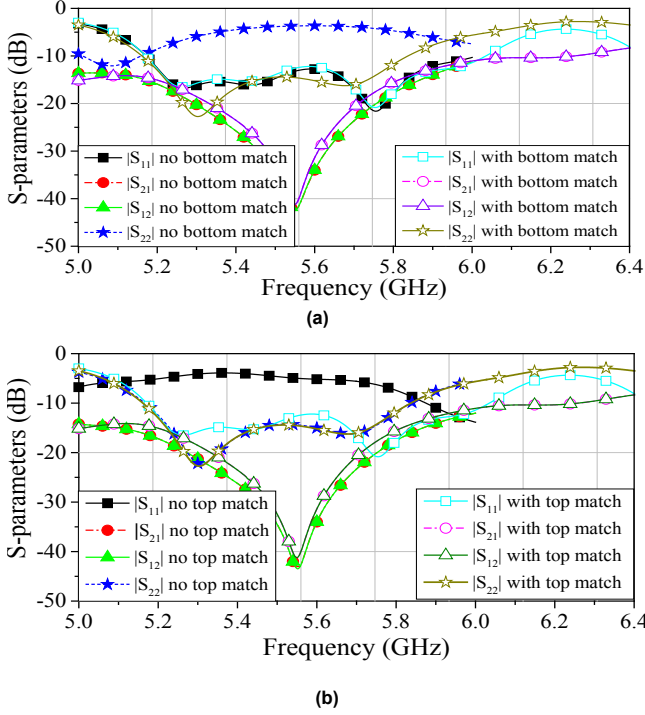
C. DCPOA Parametric study and analysis

The length of the slots mainly determines the frequency of the radiation in the improved DCPOA. The ideal length of the slots is $\lambda_0 / 2$. The slot pairs are the same [13]. However, in order to have a wider bandwidth and to maximize the power distribution amongst the four rings of slot pairs, the performance was optimized by setting $a_1 =$ 37.2 mm, $a_2 = 40.7$ mm and $a_3 = 39.4$ mm. This choice facilitates a good balance of the RHCP and LHCP power radiated by each of the four rings of slot pairs. Thus, the power radiated by the system in the horizontal direction has a high directivity [15]. Note that this DCPOA is a traveling wave antenna with good isolation between the RHCP and LHCP ports and thus achieves very good polarization diversity.
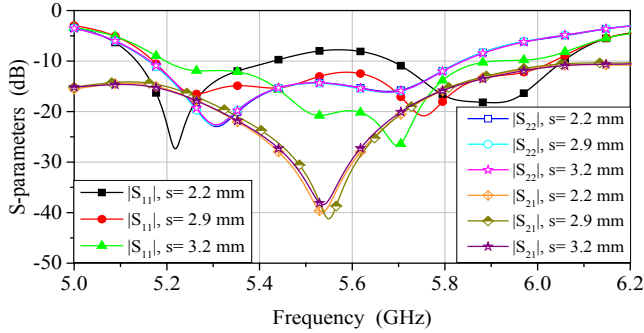
(i) Impedance matching rings in the improved DCPOA

The presence of the impedance matching metal rings is very important to achieve a large bandwidth [13]. The bottom set of rings are associated with the RHCP port 2 as shown in Fig. 3(c). Their optimized design was achieved using equivalent microwave circuits with parallel branches. These rings are particularly important to the impedance bandwidth of port 2. In Fig. 5(a), the $|S_{22}|$ values are found

to be very poor if the bottom impedance matching rings are removed, i.e., $|S_{22}|$ becomes greater than -10 dB from 5.2 to 6 GHz. On the other hand, the other S parameters, i.e., $|S_{11}|$, $|S_{21}|$ and $|S_{12}|$, remain essentially unchanged. The impedance matching rings allow much more of the channeled power to enter port 2 and, hence, to be radiated away from the slot pairs from the bottom to top of the array.

(a)

(b)

FIGURE 5. Comparison of the S parameters between the cases with and without matching rings. (a) Bottom matching rings case. (b) Top matching rings case.

FIGURE 6. Comparison of the S parameters: $|S_{11}|$, $|S_{22}|$ and $|S_{21}|$, between the cases with different slot widths, s, in the ring gap 's'.

Similarly, there are also impedance matching rings associated with the LHCP port 1 near the top, as shown in Fig. 3(c). They were optimized with similar methods to significantly improve the impedance bandwidth of port 1. The comparison between the cases with and without the top impedance matching rings is shown in Fig. 5(b). The $|S_{11}|$ values become worse if the top impedance matching rings are removed. On the other hand, the other S parameters, i.e., $|S_{21}|$, $|S_{12}|$ and $|S_{22}|$, remain essentially unchanged. As

with the bottom set, these top impedance rings allow more power to enter port 1 and to be radiated away from the slot pairs from the top to the bottom of the array.
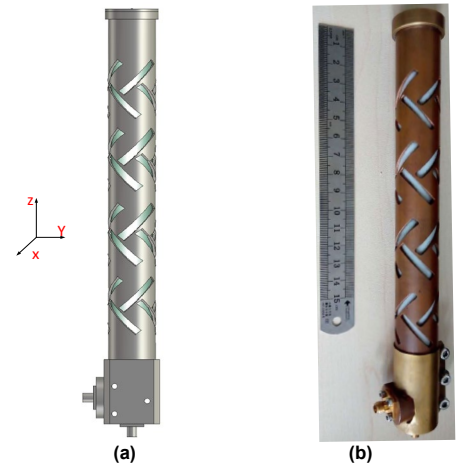
(ii) Impact of the width of the ring gap 's'

The width, s, of the ring gap 's' is the key parameter for adjusting the impedance bandwidth of the LHCP port 1. This ring gap controls the power flow from port 1 into the channel feeding the slot array. As shown in Fig. 6, the impedance bandwidth of port 1 is poor when $s = 2.2$ mm, and becomes better when $s = 2.9$ mm. However, it becomes narrower when s is increased further to 3.2 mm. Clearly, the $|S_{11}|$ values are very sensitive to the value of s. In contrast, the $|S_{21}|$ and $|S_{22}|$ values remain almost unchanged when s varies from 2.2 to 3.2 mm as shown in Fig. 6. This feature occurs because the ring gap 's' is far away from the RCHP port 2. The power input into the channels from port 2 is radiated out away from the slot arrays on the outside metal shell. Only a tiny amount of residual power will re-enter the ring gap 's' and then propagate through the ITCC to port 1.

D. Experimental verification and analysis

The optimized design parameters are listed in Table I. The improved DCPOA was fabricated; it is shown in Fig. 7.

TABLE I
OPTIMIZED PARAMETERS OF THE IMPROVED DCPOA

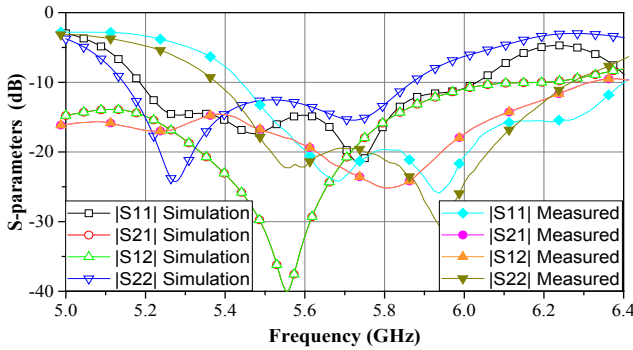| Parameter	Value (mm)	Parameter	Value (mm)	Parameter	Value (mm)
D_1	31.1	D_3	9.6	x_1	6.3
x_2	7.0	x_3	7.2	x_4	14.2
x_5	9.8	x_6	2.7	l_0	30.1
l_1	17	l_2	6.3	l_3	3.1
l_4	201.3	a_0	23.0	a_1	37.2
a_2	40.7	a_3	39.4	s	2.9
r_1	2.95	r_2	4.2	r_3	5.2
r_4	6.8	r_5	7	r_6	2.63

(a)   **(b)**

FIGURE 7. The optimized design of the dual circular polarization omnidirectional antenna. (a) Simulation model. (b) Fabricated prototype.

The outside material of the slot array is copper, and the TFS is realized with brass. These parts are connected with a copper sleeve and are then welded together. Its impedance bandwidth was measured with an Agilent PNA Network Analyzer (E8361C), and its radiation performance was measured in a far-field anechoic chamber.

(i) S- parameters

The measured return loss and isolation curves of the fabricated improved DCPOA are given in Fig. 8. The impedance bandwidth ($|S_{11}| < $ -10 dB) of the LHCP antenna is 970 MHz, from 5.43 to 6.4 GHz. When compared to the best simulation results in Fig. 6 (curves with $s = 2.9$ mm), the measured available band is shifted about 200 MHz to higher frequencies. Similarly, the measured impedance bandwidth with $|S_{22}| < $ -10 dB for the RHCP antenna is 890 MHz over 5.38 to 6.27 GHz. This available band also moved about 200 MHz to higher frequencies. The isolation between these two CP antenna ports, i.e., with $|S_{21}|$, $|S_{12}| < $ -10 dB, is from 5.0 to 6.4 GHz. These bandwidths are in reasonable agreement with their simulated values. Nevertheless, it is clear that the frequency at which the maximum isolation occurs has also moved to 5.813 GHz,

FIGURE 8. The measured and the simulated $|S_{11}|$, $|S_{12}|$, $|S_{22}|$ results of the improved DCPOA with its T-shaped feed structure.
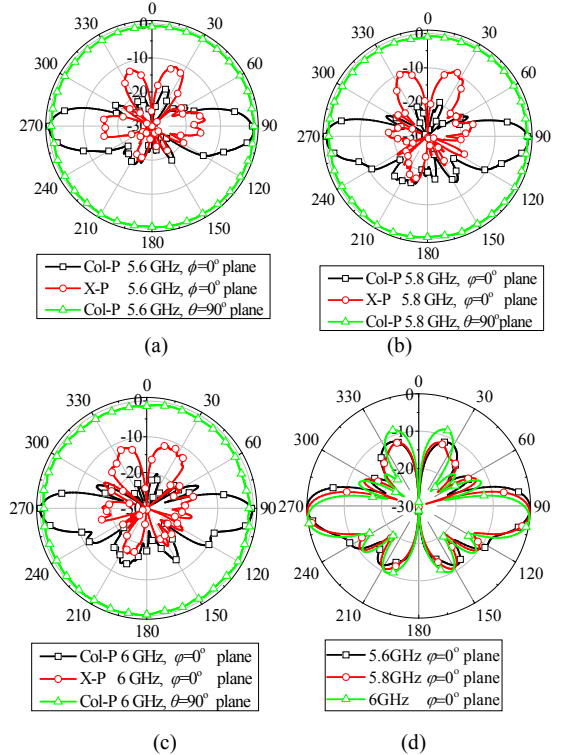
about a 250 MHz shift higher than the best simulation result in Fig. 6.

The differences between the simulated and measured results are attributed mainly to fabrication errors. The improved DCPOA is a complicated structure. It had to be divided into several parts to be fabricated. This included, for instance, the outer slot arrays, the metal shell of the TFS, and the ITCC. The TFS was cut into two parts along its axis to manufacture it. These pieces were then combined and squeezed together with a cooper sleeve. This structure left a minute gap, which affected the antenna's working band. Moreover, the width and the girth of the slots on the outer shell are very closely related to their resonance frequencies. In the simulation model shown in Fig. 7(a), the slot was obtained by a Boolean subtraction operation of a tilted rectangle and the cylindrical shell. However, the real slots on the shell were engraved with a milling cutter. As a result, the corners of the slots are arcs, not right angles.

This decreased the girth of the slots, reducing their electrical lengths. This decrease moves their resonance frequencies to a higher band. Furthermore, the minimum width between two neighboring slots has some variance from the fabrication process, again from the corner shape of the slots. It is at these points that a bottleneck of the surface current arises, again impacting their resonance frequencies. Finally, the medium filling the coaxial cylinder structure is Teflon. We set its relative permittivity to be $\varepsilon_r = 2.1$ in the simulation models. In reality, the actual value of real Teflon varies some around this value. This further adds to the differences between the measured and simulated results.

(ii) Far field of LHCP antenna

The measured normalized far fields of the LHCP antenna excited from the LCHP port 1 at $f = 5.6$, 5.8 and 6.0 GHz are shown in Figs. 9(a)−9(c), respectively. The main beam direction is almost at $\theta = 90^o$ for each frequency. Similarly, the far-field pattern in the azimuthal φ-plane ($\theta = 90^o$) is close to a circle, i.e. it is essentially omnidirectional in the horizontal plane with only small variations. The cross polarization levels in Fig. 9(a) at $f = 5.6$ GHz are 15 dB smaller than the main beam. The measured LHCP beams become fat within the range $\theta = 110^o$-120° for both 5.6 and

FIGURE 9. Far-field patterns of the omnidirectional LHCP antenna of the TFS-enabled PDA. The normalized measured far-fields results at (a) f = 5.6 GHz, (b) f = 5.8 GHz, and (c) f = 6.0 GHz. (d) The corresponding normalized simulated co-polarization patterns in ϕ=0° plane.

5.8 GHz. The reason is that the radiated power distribution from the slots pairs along the coaxial cylinder axis is not uniform. As shown in Fig. 4(a), the power flow distribution
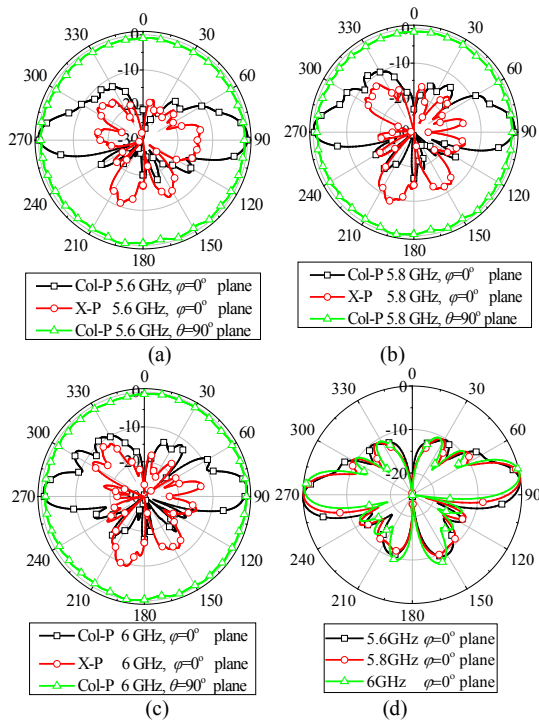
is much larger in the rings of slots near the top of the antenna than those close to its bottom. This inhomogeneous distribution results in the asymmetrical beam in the θ-plane. On the other hand, the cross polarization level is 17.5 dB smaller than the main beam at $\theta = 90^\circ$ at 5.8 GHz.

In contrast, the inhomogeneous power distribution causes the first clear side beam in the direction $\theta = 120^\circ$ at f = 6.0 GHz in Fig. 9(c). This effect arises because the electrical length between the rounded slots becomes larger as the frequency increases from 5.6 to 6.0 GHz. As a result, a new null is introduced at $\theta = 110^\circ$, and the side beam is clearly split.

The measured far-field patterns of the LHCP antenna in the $\varphi = 0^\circ$ plane at 5.6, 5.8 and 6.0 GHz are shown in Fig. 9(a)-9(c). They are similar to the simulated ones given in Fig. 9(d).

(iii) Far field of the RHCP antenna

The normalized measured far-field RHCP radiation patterns of the antenna when port 2 is excited at f = 5.6, 5.8 and 6.0 GHz are shown in Figs. 10(a)-10(c), respectively. The main beam is pointed in the horizontal direction ($\theta = 90^\circ$) and the far-field pattern in the azimuthal φ-plane ($\theta = 90^\circ$) is omnidirectional with little variance for each of these frequencies. The cross polarization level at f = 5.6 GHz is about 15 dB smaller than the main beam value at $\theta = 90^\circ$. The cross polarization level at f = 5.8 and 6.0 GHz is 20 dB smaller than the main beam value at $\theta = 90^\circ$.

The main beams are all asymmetrical relative to the azimuthal plane. In Fig. 10(a), the main beam is fatter above it than it is below it. In Fig. 10(b), the main beam slightly splits near $\theta = 60^\circ$. In Fig. 10(c), the main beam clearly has a split around $\theta = 60^\circ$. The reason is related to the issues discussed above. As shown in Fig. 4(b), the power flow distribution is non-uniform along the z-axis; it is much larger in the lower three rings of slots. Moreover, the electrical distances between them become larger as the frequency increases from 5.6 to 6.0 GHz. Both aspects cause the first side beam to become split out from the main beam.

The measured far-field patterns of the RHCP antenna in the $\varphi = 0^\circ$ plane at 5.6, 5.8 and 6.0 GHz are shown in Figs. 10(a)-10(c). They are similar to the simulated ones given in Fig. 10(d).

(iv) Radiation performance of the improved DCPOA

The simulated radiation efficiencies and realized gains of the LHCP and RHCP antennas are shown in Fig.11. The radiation efficiency of the LHCP antenna is larger than 0.8 from 5.13 ~ 6.05 GHz; the corresponding realized gain is 5.0 ~ 7.0 dBi taking into account the reflection coefficient values shown in Fig.8 over this set of frequencies. Similarly, the simulated frequency band of the RHCP antenna with radiation efficiencies being larger than 0.8 is from 5.11 ~ 5.9 GHz. The corresponding simulated realized
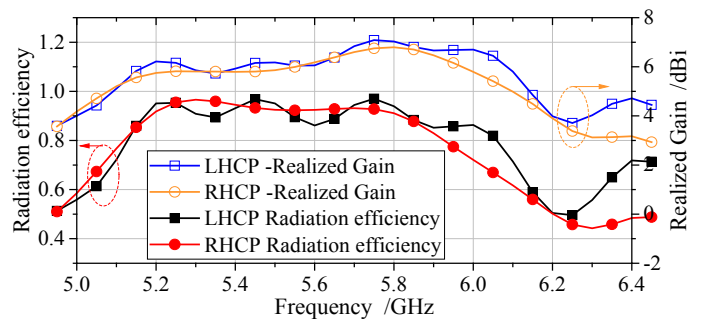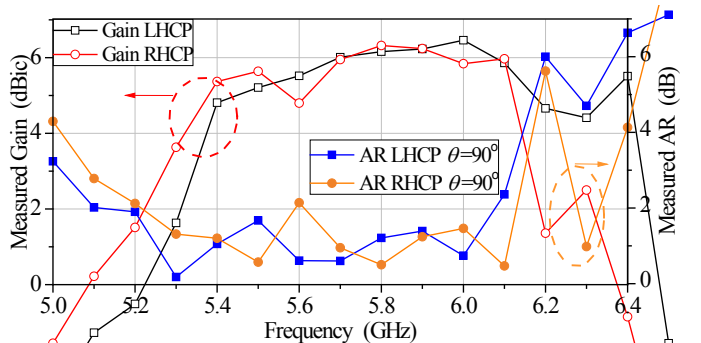

FIGURE 10. Far-field patterns of the omnidirectional RHCP antenna of the TFS-enabled PDA. The normalized measured far-fields results at (a) f = 5.6 GHz, (b) f = 5.8 GHz, and (c) f = 6.0 GHz. (d) The corresponding normalized simulated co-polarization patterns in ϕ=0° plane.

FIGURE 11. Simulated radiation efficiency and realized gain values of the LRHCP and RHCP antennas as functions of the source frequency.

FIGURE 12. Measured gain and AR values of the LRHCP and RHCP antennas as functions of the source frequency.

gain values are 5.0 ~ 7.0 dBi. The values with $|S_{22}|$< -10dB in Fig.8 are from 5.15 ~ 5.85 GHz.

The measured gain and axial ratio results of the improved DCPOA are shown in Fig. 12. Exciting the LHCP port 1, one finds the CP band where AR < 3 dB in the main beam direction is from 5.02 to 6.12 GHz. The corresponding gain values are from 0.3 to 6.46 dBic, the gain peak being obtained at 6.0 GHz. Taking into account the impedance band ($|S_{11}|$ < -10 dB) in Fig. 8 and the LHCP band (AR < 3 dB) in Fig. 12, the available overall working band is 5.43-6.12 GHz, and the gain levels available in it are 5.0 to 6.46 dBic.

Similarly, when the RHCP port 2 is excited, the measured CP band with AR < 3 dB in the main beam direction is from 5.1-6.37 GHz except for a small interval from 6.15-6.25 GHz. The measured gain of the RHCP antenna is 0.2 to 6.32 dBic in this CP band. Considering the impedance band ($|S_{11}|$ < -10 dB) in Fig. 8 and the RHCP band (AR < 3 dB) in Fig. 12, the available working RHCP band is 5.38-6.15 GHz, and the gain values in it are from 4.8 to 6.32 dBic.

The measured main LHCP and RHCP bands are shifted about 250 MHz to higher frequencies from their simulated values. As noted above, the reasons are mainly due to the various fabrication and filling medium errors.

E. Comparison with other dual CP antenna

The improved DCPOA prototype and other reported dual CP antennas are compared in Table II. The improved DCPOA achieves a measured impedance bandwidth of 16.4% for its LHCP antenna and 15.28% for its RHCP antenna. The isolation between the two ports is -25 to -10 dB within their operating bands. The gain and AR values of both antennas are shown in Fig. 12. The peak LHCP gain is

TABLE II
COMPARISON OF DUAL CP OMNIDIRECTIONAL ANTENNA

Ref.	CP		BWs	CP band	Omni-direction	size	Gain (dBic)
[24]	CP/switch		19.8%	20%	Good	$0.93\lambda\times 0.93\lambda\times 0.024\lambda$	< 2.5
[25]	CP/switch		18%	22%	Good	$0.55\lambda\times 0.44\lambda\times 0.44\lambda$	0.1-0.4
[26]	CP		41%	45%	Good	$1.625\lambda\times 0.38\lambda\times 0.38\lambda$	1.5-4.5
[15]	DCP	LHCP	16.4%	18.1%	Poor	$3.5\lambda\times 0.6\lambda\times 0.6\lambda$	4-6
		RHCP	16.4%	18.1%	Poor	$3.5\lambda\times 0.6\lambda\times 0.6\lambda$	4-6
This work	DCP	LHCP	16.4%	21.35%	Good	$4.3\lambda\times 0.6\lambda\times 0.6\lambda$	5-6.46
		RHCP	15.28%	20.58%	Good	$4.3\lambda\times 0.6\lambda\times 0.6\lambda$	4.8-6.32

from 5.0 to 6.46 dBic while for the RHCP gain it is from 4.8 to 6.32 dBic over their working bands. Thus, it was confirmed that the prototype antenna has very good dual CP omnidirectional character in the horizontal, azimuthal plane.

IV. TFS-enabled Space Diversity Antenna

The development of base stations located on air-based platforms, such as balloon-carried ones, will enable covering wider regions on the earth and transmitting power with less attenuation than traditional base stations located on the ground. For this concept to be successful, it is necessary that the corresponding terminal antennas on the ground should achieve hemispherical coverage to connect seamlessly both to the base station in the sky and to the base stations located in the network on the ground. The
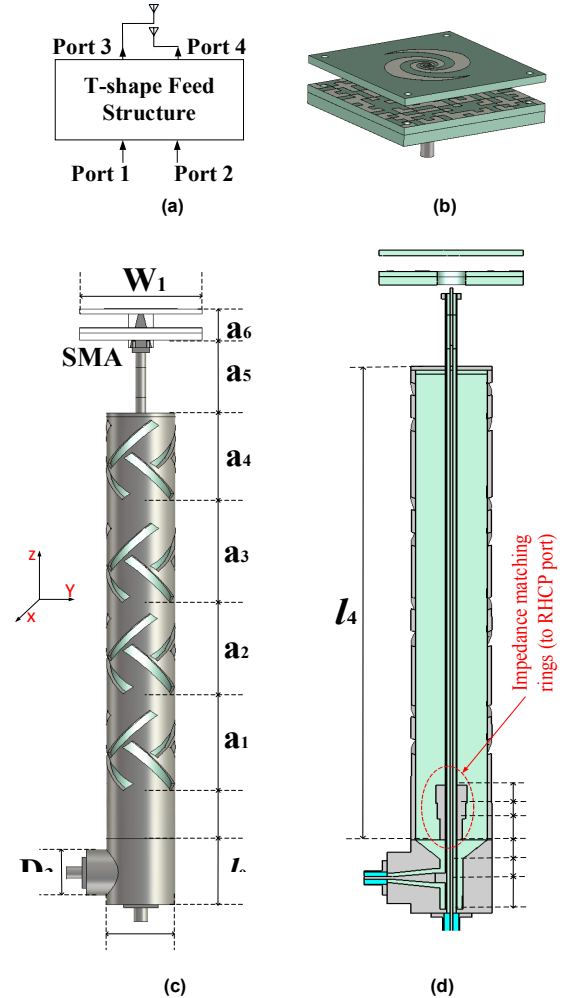

FIGURE 13. The T-shaped feed CP slots antenna with embedded coaxial line to feed the directional planar equiangular spiral antenna on the top. (a) Block diagram. (b) The low-profile, wide bandwidth, directional planar equiangular spiral antenna (DPESA) on top of the structure has CP characteristics [21]. (c) 3D view. (d) Cross-sectional view through a vertical cut.

reported SDA is a very good approach to enable this scenario. The SDA radiates different far field patterns from different ports overcoming the dark fringes of the coverage, as well as multipath and channel fading in the anticipated wireless communication networks.

A. The principle of the SDA with TFS

The SDA shown in Fig. 13 consists of a low-profile directional, planar equiangular spiral antenna (DPESA) that radiates upwards, orthogonal to it, and an omnidirectional RHCP antenna that radiates primarily in the horizontal plane of the SDA structure. The low-profile DPESA is mounted on top of the SDA structure and has high gain into the top space [21]. The omnidirectional RHCP antenna achieves high gain in the horizontal plane. Thus, complete hemispherical coverage is achieved. The TFS is used to feed these two antennas. Port 1 directly feeds the low-profile DPESA on the top of the structure, and port 2 feeds the OCPSA. The ITCC runs through the structure to the top cap of the coaxial slot array antenna without the presence of the ring gap 's'. This configuration is equivalent to port 3 being extended to feed the low-profile DPESA. The TFS, OCPSA, and low-profile DPESA combination was optimized to achieve the desired performance characteristics.

B. SDA Structure and Performance

The ITCC has a characteristic impedance of 50 Ω; it completely passes through the center of the OCPSA to be connected directly to port 1 and the low-profile DPESA. The DPESA is an optimized version of the previously reported planar directional antenna with a 50 Ω SMA adaptor port [21]. The radiation segment of this antenna is an equiangular planar spiral structure. There are two parasitic layers consisting of rotationally symmetry structures, one being an optimized digital-code metasurface [22], [23] located beneath the radiating element. The DPESA also has a rectangular metal bottom that acts as its ground plane. Furthermore, the metal shell of the ITCC is regarded as the center wire of the OCPSA fed by port 2. Consequently, the feeding channel from port 1 to the low-profile DPESA and the feeding channel from port 2 to the OCPSA are physically isolated.

When a signal is fed into the SDA from port 2, it propagates through the TFS entering the OCPSA from its bottom and continues propagating to its top. This is similar to the case of the RHCP antenna of the improved DCPOA discussed in Section III. Similarly, it is loaded at its bottom with impedance matching rings to improve the impedance bandwidth of port 2. The bottom impedance matching rings are optimized to attain as small a return loss as possible. The distance of the fourth ring of slot pairs from the top metal cap is also adjusted for good impedance matching. The space between the outer conductor of the ITCC and the

outer conductor shell of the antenna is again filled with Teflon. This SDA was simulated and optimized with CST. The optimized design parameters are given in Table III.

TABLE III
OPTIMIZED DESIGN PARAMETERS OF THE SPATIAL DIVERSITY ANTENNA

Parameter	Value (mm)	Parameter	Value (mm)	Parameter	Value (mm)
D_1	25	D_3	19	a_1	39.7
a_2	37.5	a_3	42.25	a_4	35.4
a_5	30	a_6	12.85	l_0	27
l_1	11.5	l_2	7	l_3	7
l_4	174.6	x_1	7.8	x_2	5.8
x_3	6.5	W_1	44.2		
r_1	2.9	r_2	4.0	r_3	5.2

C. Experimental verification and analysis

A prototype of the SDA was fabricated and tested. Its
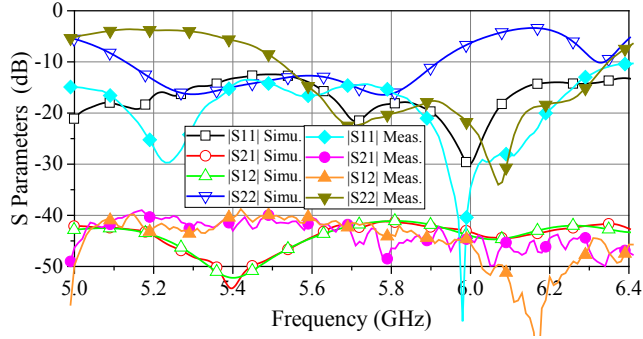

FIGURE 14. The optimized CP SDA. (a) Simulation model. (b) Fabricated prototype.

simulation model and the fabricated system are shown in Fig. 14. Its bandwidth was measured with an Agilent PNA Network Analyzer E8361C. Its radiation performance was measured in the far-field anechoic chamber.

(i) S parameters

The measured return loss and isolation curves of the fabricated SDA are shown in Fig. 15. The OCPSA achieves an impedance bandwidth of 850 MHz from 5.5 to 6.35 GHz, a fractional bandwidth of about 14.35%. The measured impedance bandwidth of the low-profile DPESA is wider than 1400 MHz, from 5.0 to 6.4 GHz. The measured isolation between the two ports is approximately larger than 40 dB from 5.0 to 6.4 GHz. It is noted that the measured impedance band of the RHCP omnidirectional antenna
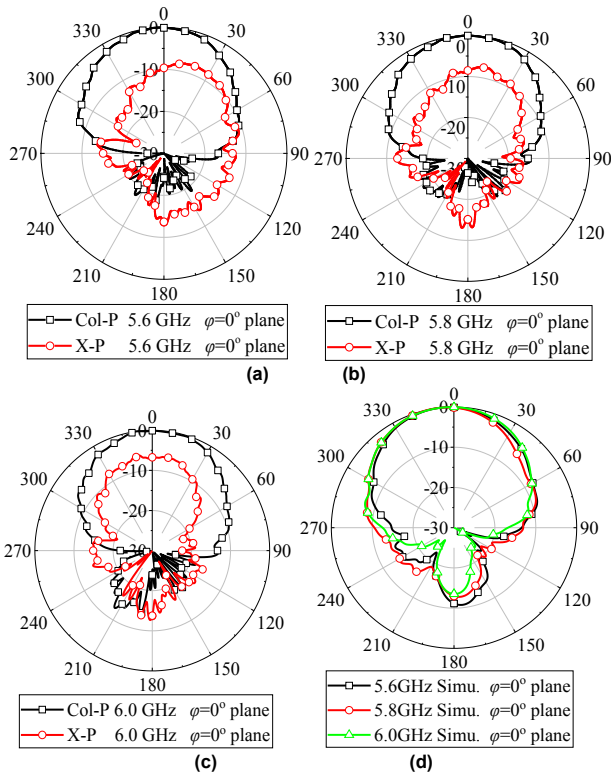
shifts about 380 MHz to higher frequencies. Again, it has been determined through simulation and further measurements that this frequency offset is due to the manufacturing errors of the TFS, the slot array on the outer shell, the distance of separation errors between the slots, and the real nature of the Teflon filling.

FIGURE 15. The measured and simulated |S_{11}|, |S_{12}|, |S_{21}|, |S_{22}| results of the TFS-enabled SDA.

(ii) SDA far- field performance

The normalized measured far-field patterns of the low-profile DPESA excited from port 1 at f = 5.6, 5.8 and 6 GHz are given in Figs. 16(a)-16(c), respectively. The main beams point upwards; their 3 dB beam widths in the φ = 0° plane are 66.5°, 72° and 69°, respectively. It is observed that the cross-pol level is somewhat higher than desired. The equiangular planar spiral structure of the DPESA is a UWB structure that radiates bidirectionally. To achieve the desired wideband directional radiation with a low profile structure, we introduced two parasitic layers. They are rotationally symmetry structures, one being an optimized digital-code metasurface [22], [23] located beneath the radiating element. The DPESA also has a rectangular metal bottom that acts as its ground plane. The parasitic layers and the ground have been stacked in a such manner that when the antenna is excited, the upward radiation field and the fields reflected from these structures achieve the correct phase to mitigate the back radiation. Unfortunately, the trade-off with this stacking arrangement is a degradation of the CP performance [21].

In comparison to the simulated far-field patterns in Fig.16(d), the measured far-field patterns of the DPESA in its E-plane at 5.6, 5.8 and 6.0 GHz are very similar.

The corresponding normalized measured far-field patterns of the omnidirectional RHCP antenna excited from port 2 are shown in Figs. 17(a)-17(c). The main beam points along $\theta = 90°$ in the horizontal plane; the far-field radiation patterns in the azimuthal φ-plane ($\theta = 90°$) are
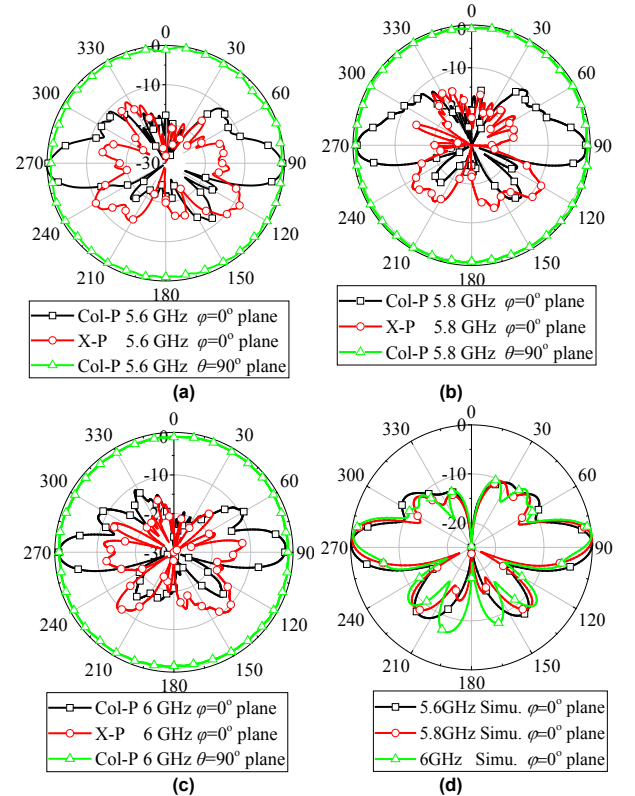

FIGURE 16. The normalized measured far field patterns of the DPESA of the TFS-enabled SDA at (a) f = 5.6 GHz, (b) f = 5.8 GHz, and (c) f = 6.0 GHz. (d) The corresponding normalized simulated co-polarization patterns of the DPESA in the φ=0° plane.
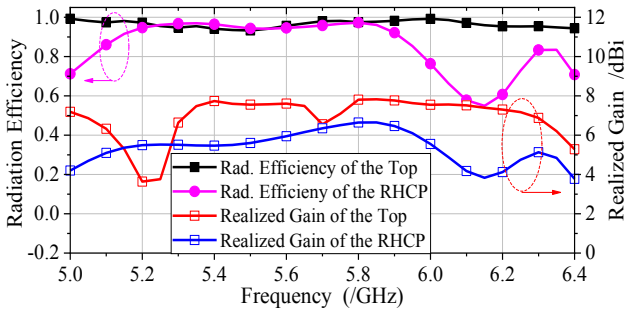

FIGURE 17. Far-field patterns of the omnidirectional RHCP antenna of the TFS-enabled SDA. The normalized measured far-fields results at (a) f = 5.6 GHz, (b) f = 5.8 GHz, and (c) f = 6.0 GHz. (d) The corresponding normalized simulated co-polarization patterns in φ=0° plane.

omnidirectional with little variation. The cross polarization levels in Figs. 17(a)-17(c) are, respectively, about 18, 30, and 15 dB smaller than the main beam value at $\theta = 90^o$. These measured far-field patterns are quite similar to their simulated values shown in Fig. 17(d). The measured far-field patterns nicely coincide with those of the RHCP omnidirectional antenna of the improved DCPOA described in Section III.
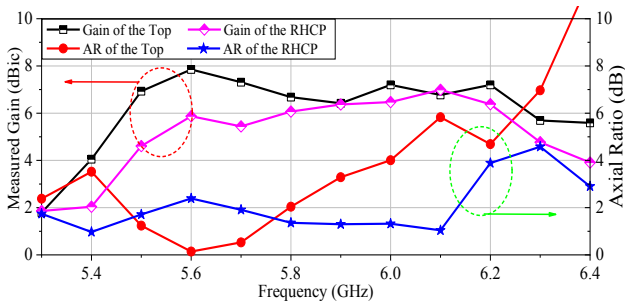
(iii) SDA radiation performance

The simulated radiation efficiency and realized gain values of the top DPESA (excited from port 1) and the RHCP antenna (excited from port 2) are shown in Fig.18. The simulated radiation efficiency of the top DPESA is larger than 0.9 from 5.0 to 6.4 GHz. The frequency range is the same as the simulated impedance band defined by $|S_{11}|$, $|S_{22}| < -10$ dB in Fig.15. The radiation efficiency is larger than 0.8 from 5.05 to 6.0 GHz for the RHCP antenna. The corresponding simulated realized gain values are from 3.63 to 7.82 dBi.

The measured gain and axial ratio values of the SDA are shown in Fig. 19. The measured gain of the DPESA (excited from port 1) is from 4.0 to 7.8 dBic in the frequency interval from 5.4 to 6.4 GHz. The maximum gain occurs at 5.6 GHz. The CP band (AR < 3 dB) is about 450 MHz (5.45-5.9 GHz). The measured CP band of the RHCP antenna is about 867 MHz from 5.3 to 6.167 GHz. The corresponding gain is from 2.0 to 6.99 dBic in this band.

FIGURE 18. The simulated radiation efficiency and the realized gain of the SDA antenna's omnidirectional RHCP system and its low-profile DPESA.

FIGURE 19. The measured gain and AR values of the SDA antenna's omnidirectional RHCP system and its low-profile DPESA.

The maximum gain occurs at 6.1 GHz. Considering the impedance band ($|S_{11}| < -10$ dB) in Fig. 15 and the RHCP band (AR < 3 dB) in Fig. 19, the available common working band is 5.5 to 6.167 GHz and the associated gain is from 4.4 to 6.99 dBic. Again, these measured results are almost the same as those of the RHCP omnidirectional antenna of the improved DCPOA discussed in Section III.

D. Comparison with other spatial diversity antennas

The performance of our SDA prototype and other reported space diversity antennas are compared in Table IV. The reported SDA prototype has a much larger bandwidth and comparable gain levels for both its combined directional and omnidirectional performance when compared to the reported designs. It is noted that the reported SDA is spatially diverse with hemispherical coverage that is suitable to a wide variety of wireless applications.

V. Conclusion

TABLE IV
COMPARISON OF SDA

Ref.	Bands (GHz)	Polari-zation	Pattern Type	Size （mm³）	Gain (dB)
[27]	1.7-2.7 4.7- 8.5	LP	directional	50×17×0.8	< -0.31
[28]	27.56-28.4 37.8-38.9	RHCP	directional	3 × 4 ×0.254	7.2
[29]	4.6% 0.85 - 0.89	LHCP	end fire	229.2×26.2× 26.2	2.5
This work	14.35% 5.5 - 6.35	RHCP	Omni-directional	243 ×44 ×44	< 6.99
	Wide band	Top:RHCP	directional		< 7.8

In this paper, PDA and SDA systems enabled by a novel compact 4-port TFS were reported. Both of these diversity antennas are fed from their bottoms, which makes them convenient for mounting on top of structures. Prototypes of both were fabricated and tested.

The reported improved DCPOA achieved a measured fractional impedance bandwidth of 16.4% for its LHCP and 15.28% for its RHCP subsystems. Both the measured $|S_{11}|$ and $|S_{22}|$ values were lower than -10 dB between 5.43 to 6.27 GHz. The measured isolation between the two ports was -25 to -10 dB within the same band. The measured LHCP gain was 5.0 to 6.46 dBic while the RHCP gain was 4.8 to 6.32 dBic in the same band. The manufactured prototypes achieved very good dual CP properties and omnidirectional radiation patterns in their horizontal planes.

Similarly, the measured fractional impedance bandwidth of the reported SDA was about 14.35%, ranging from 5.5 to 6.35 GHz. The measured isolation between the two ports

was larger than 40 dB within the same band. The measured gain of its low-profile DPESA (excited from port 1) was 4.0 to 7.8 dBic in its working band. Its main beam direction pointed in the zenith direction. The measured CP band of its OCPSA (excited from port 2) was about 867 MHz. Its measured gain was 4.4 to 6.99 dBic in its working band, i.e., for frequencies with $|S_{11}|$ < -10 dB and AR < 3 dB. This RHCP antenna was measured to have very good omnidirectional CP radiation in its horizontal plane.

The demonstrated performance characteristics of the PDA and SDA systems make both of them attractive to a variety of current and upcoming wireless communication applications.

Acknowledgement

REFERENCES

[1] Y. Kihc, M. Koca, and E. Ananm, "Space-time-polarization diversity in multiple-input multiple-output communication systems, *IEEE AFRICON 2009*, Nairobi, Kenya, Sept. 23 – 25, 2009.

[2] W. Lee and Y. Yu, "Polarization diversity system for mobile radio," *IEEE Trans. Commun.*, vol. 20, no. 5, pp. 912-923, Oct. 1972.

[3] R. U. Nabar, H. Bölcskei, V. Erceg, D. Gesbert, and A. J. Paulraj, "Performance of multiantenna signaling techniques in the presence of polarization diversity," *IEEE Trans. Signal Process.*, vol. 50, no. 10, pp. 2553-2562, Oct. 2002.

[4] G. Maral and M. Bousquet, *Satellite Communication Systems*, Chichester, England: John Willey & Sons, 2002.

[5] M. Richharia, *Satellite Communication Systems*, New York: McGraw Hill, 1999.

[6] G. Chenhu, J. Geng, H. Zhou, J. Li, L. Liu, Y. Chen, Y. Liang, X. Liang, W. Zhu, and R. Jin, "A half-space covered antenna for air-ground communication," *IEEE Asia-Pacifc Conference on Antennas and Propagation*, Xi'an, China, Oct. 16-19, 2017.

[7] E. Fishler, A. Haimovich, R. S. Blum, D. Chizhik, and R. A. Valenzuela, "Spatial diversity in radars-models and detection performance," *IEEE Trans. Signal Process.*, vol.54, no. 3, pp. 823-838, Mar. 2006.

[8] A. M. Hunter, J. Andrews, and S. Weber, "Transmission capacity of ad hoc networks with spatial diversity," *IEEE Trans. Wireless Commun.*, vol. 7, no. 12, pp. 5058-5071, Dec. 2008.

[9] S. N. Diggavi, N. Al-Dhahir, A. Stamoulis, and A.R. Calderbank, "Great expectations: The value of spatial diversity in wireless networks," *Proc. IEEE*, vol. 92, no. 2, pp. 219-270, Feb. 2004.

[10] B. Li, S. W. Liao, and Q. Xue. "Omnidirectional circularly polarized antenna combining monopole and loop radiators." *IEEE Antennas Wireless Propag. Lett.*, vol. 12, pp.607-610, Apr. 2013.

[11] X.-L. Quan and R. L. Li. "Broadband dual-polarized omnidirectional antennas," *Antennas and Propagation Society International Symposium (APSURSI), 2012 IEEE*, vol.11, no.4, Chicago, IL, USA, July, 8-14, 2012, pp.1-2.

[12] Y. M. Cai, S. Gao, Y. Yin, W. Li, and Q. Luo, "Compact-size low-profile wideband circularly polarized omnidirectional patch antenna with reconfigurable polarizations," *IEEE Trans. Antennas Propag.*, vol. 64, no. 5, pp. 2016-2021, May. 2016.

[13] B. Zhou, J. Geng, X. Bai, L. Duan, X. Liang, and R. Jin, "An omnidirectional circularly polarized slot array antenna with high gain in a wide bandwidth," *IEEE Antennas Wireless Propag. Lett.*, vol. 14, pp. 666-669, 2015.

[14] B. Zhou, J. Geng, X. Liang, and R. Jin, "A compact omnidirectional CP coaxial slots antenna," *2015 IEEE 6th International Symposium on Microwave, Antenna, Propagation, and EMC Technologies (MAPE)*, Shanghai, China, Oct., 28-30, 2015, pp. 821-822.

[15] B. Zhou, J. Geng, Z. Li, W. Wang, X. Liang and R. Jin, "Dual circularly polarized omnidirectional antenna with slot array on coaxial cylinder," *Int. J. Antenn. Propag.*, vol. 2015, Article ID 127820, pp.1-7, http://dx.doi.org/10.1155/2015/127820

[16] B. Zhou, J. Geng, X. Liang, R. Jin, and G. Chenhu, "Omnidirectional circularly polarized antenna with high gain in wide bandwidth," in *Modern Antenna Systems*, Intech, 2016, ISBN 978-953-51-4943-9.

[17] G. Chenhu, J. Geng, L. Liu, H. Zhou, X. Zhao, Y. Liang, X. Liang, W. Zhu, and R. Jin, "A circular truncated cone slot antenna with circular polarized conical beam," *2017 IEEE International Symposium on Antennas and Propagation & USNC/URSI National Radio Science Meeting*, San Diego, CA, USA, July 9-14, 2017, pp. 1533-1534.

[18] G. Chenhu, J. Geng, B. Zhou, J. Li, Y. Chen, W. Zhu, R. Jin, and R. W. Ziolkowski, "A T-shaped feed structure to enhance the performance of a polarization diversity antenna,"*2017 IEEE International Symposium on Antennas and Propagation & USNC/URSI National Radio Science Meeting*, San Diego, CA, USA, July 9-14, 2017, pp. 2143-2144.

[19] [Online] http://www.cst.de/Content/Company/Academic.aspx

[20] T. Weiland, "Time domain electromagnetic field computation with finite difference methods," *Int. J. Numer. Modelling V Electron. Netw., Devices Fields*, vol. 9, no. 4, pp. 295–319, Jul. 1996.

[21] X. Zhao, J. Geng, R. Jin, Y. Jin, X. Liu, and W. Yin, "Topological design of planar circularly polarized directional antenna with low profile using particle swarm optimization," *Int. J. Antenn. Propag.*, vol. 2017 (2017), Article ID 4983724, 12 pages

[22] H. Wu, J Geng, R. Jin, J. Qiu, W. Liu, J. Chen, S. Liu, "An Improved Comprehensive Learning Particle Swarm Optimization and Its Application to the Semiautomatic Design of Antennas", *IEEE Trans. Antennas Propag.*,vol.57, no.10, July 2009, pp. 3018-3028.

[23] J. Geng, R. Jin, X. Liang,H. Wu, S. Ye, B. Zhou, X. Tao, "The study on the antenna optimization" , *PIERS*, Xi'an, China, 23 –28, March. 2010.

[24] Y.-M. Cai, S. Gao, Y. Yin, W. Li, and Q. Luo, "Compact-size low-profile wideband circularly polarized omnidirectional patch antenna with reconfigurable polarizations," *IEEE Trans. Antennas Propag.*, vol. 64, no. 5, May 2016, pp. 2016-2021.

[25] Y. Fan, Y. Cui, and R. Li, "Polarization reconfigurable omnidirectional antenna using crossed dipoles," *2015 IEEE International Symposium on Antennas and Propagation & USNC/URSI National Radio Science Meeting*, Vancouver, BC, Canada, July 19-14, 2015, pp. 2371-2372.

[26] X. Quan, R. Li, and M. M. Tentzeris, "A broadband omnidirectional circularly polarized antenna," *IEEE Trans. Antennas Propag.*, vol. 61, no. 5, pp. 2363-2370, May 2013.

[27] W. J. Krzysztofik, "Space diversity parameters of MIMO systems small antenna array for mobile terminal." *2016 10th European Conference on Antennas and Propagation (EuCAP)*, Davos, Switzerland, Apr. 10-15, 2016, pp. 1-4.

[28] H. Aliakbari, A. Abdipour, A. Costanzo, D. Masotti, R. Mirzavand, and P. Mousavi, "Performance investigation of space diversity for a 28/38 GHz MIMO antenna (applicable to mm-wave mobile network)," *2016 Fourth International Conference on Millimeter-Wave and Terahertz Technologies (MMWaTT)*, Tehran, Iran, Dec. 20-22, 2016, pp. 41-44.

[29] J. F. Gonzalez, P. Padilla, J. F. Valenzuela-Valdes, J. Padilla, and M. Sierra-Perez, "An embedded lightweight folded printed quadrifiar helix antenna: UAV telemetry and remote control systems," *IEEE Antennas Propag. Mag.*, vol. 59, no. 3, pp. 69-76, Jun. 2017.